# ON THE IMPORTANCE OF ATTENUATION IN ACOUSTIC WAVEFORM TOMOGRAPHY OF MARINE SEISMIC DATA

*A. Kurzmann, A. Przebindowska, and T. Bohlen*

**email:** *kurzmann@kit.edu*

**keywords:** *acoustic full waveform tomography, time-domain, attenuation*

## ABSTRACT

*Full waveform tomography (FWT) is a powerful imaging method to exploit the richness of full seismic waveforms. In general, complex seismic data arises from heterogeneous geology of the subsurface. In this study we investigate the applicability of acoustic FWT to marine reflection data. We focus on analyzing the impact of attenuation on the reconstruction of a P-wave velocity model by acoustic FWT.*

*Based on relaxation mechanisms of the generalized standard linear solid (GSLS) we involved attenuation into finite-difference modeling of 2D time-domain acoustic FWT. Using a homogeneous full-space the comparison of finite-difference-based waveforms and a semi-analytical solution shows a good conformity.*

*We applied acoustic FWT with and without consideration of initial attenuation information to both a 1D structured model and the 2D Marmousi model. We found that in case of marine reflection experiments with occurrence of lossy sedimentary rocks the neglection of attenuation causes an insufficient recovery of the velocity model as well as an improper fit of the observed viscoacoustic data. The maximum absolute model error between the inverted Marmousi model and the reference velocity model (optimal reference result obtained by acoustic FWT of acoustic data) is approximately 30 percent with an average absolute error of 5.7 percent. The choice of an appropriate viscoacoustic starting model, which includes a smooth quality factor model, is thus important, improves the reconstructed Marmousi P-wave velocity model and decreases the maximum absolute model error to 24 percent (with an average absolute error of 2.5 percent).*

*A successful FWT application should account for attenuation – either as a passive parameter or as subject to inversion.*

## INTRODUCTION

In the majority of FWT applications we face a multi-parameter problem, i. e., it is desirable to obtain information about seismic velocities, density and attenuation from seismic data. The aim of full waveform tomography – an iterative inversion method – is to find an optimal parameter model, e.g. a subsurface model of seismic velocities, which explains the observed seismic data, i.e., the difference of observed and synthetic data has to be minimized. Especially real data application might require the consideration of all available parameters which comprise bulk modulus and attenuation in the acoustic approximation. Attenuation affects both amplitude and phase of seismic signals, i.e., it causes amplitude modifications and dispersion resulting in strongly frequency-dependent velocity models.

Fundamental work of developing time-domain FWT (Tarantola, 1984) and including attenuation into elastic FWT was done by Tarantola (1986). His basic idea is to use causal attenuation in forward-propagation and anti-causal attenuation in back-propagation of the seismic wavefield. In frequency-domain FWT (cp. Pratt, 1999) the intrinsic attenuation is included quite easily by introducing complex velocities (Johnston,

1981). On the one hand it is used as a passive model parameter to improve the inversion for desired parameters like P-wave velocity (e. g., Brenders and Pratt, 2007). Furthermore, multi-parameter FWT involves attenuation as an additional paramater of interest. Many applications focus on synthetic investigations of velocity model improvement by recovering attenuation, explicit reconstruction of an attenuation model or mitigation of nonlinearity and ill-posedness of FWT (e. g., Hak and Mulder, 2008, 2011; Kamei and Pratt, 2008). Additionally, there are already several field data applications of FWT that account for attenuation in the frequency-domain, e.g. Hicks and Pratt (2001), Takam Takougang and Calvert (2011) and Malinowski et al. (2011). A brief overview about recent publications in this area is given by Virieux and Operto (2009). Furthermore, several authors apply additional methods to recover attenuation like asymptotic waveform inversion. This method realizes wave equation modeling by Born approximation and ray tracing (Ribodetti and Virieux, 1998; Ribodetti et al., 2004).

In conjunction with application to wide-aperture seismic field data, Malinowski et al. (2011) investigated both the influence of different initial quality factor models on acoustic frequency-domain FWT and applicability of a viscoacoustic joint inversion for P-wave velocity as well as quality factor. They conclude that viscoacoustic FWT is able to recover both parameters sufficiently. Apart from that, Mulder and Hak (2009) discuss problems of such a joint inversion.

We investigate the role of attenuation for time-domain acoustic FWT in marine reflection seismics. Especially in marine sediments the quality factor may vary from low values around $20\ \frac{1}{\mathrm{Np}}$ to high three-digit values. Resulting dispersion and amplitude modifications might be a serious problem in recovering a sufficient velocity model by acoustic FWT. Although this study concentrates on 2D acoustic FWT in the time-domain, it is also targeted to 3D applications. In contrast to high efficiency of 2D frequency-domain FWT by easy implementation of attenuation, computation of 3D frequency-domain modelings is highly demanding. Hence, in 3D FWT applications time-domain modeling is commonly used. Furthermore, advantageous time-domain features like straightforward time-windowing of data and the consideration of broad frequency bands (instead of single frequencies) are available. Based on a time-domain implementation of acoustic FWT with viscoacoustic modeling we analyze the impact of attenuation on its ability to reconstruct a proper velocity model from viscoacoustic data (whereas the influence of density is neglected). Furthermore, with respect to a reference result we quantify errors obtained from this model reconstruction including or excluding viscoacoustic modeling. For the purpose of this study we utilize synthetic but realistic marine reflection seismics experiments.

In detail this work comprises implementation of finite-difference viscoacoustic modeling in the time-domain acoustic FWT, its verification using a semi-analytical solution based on the Born approximation (Carcione et al., 1988b; Carcione, 2001; Emmerich and Korn, 1987) within a homogeneous model and application of acoustic full waveform tomography to viscoacoustic data in case of a simple 1D medium and the 2D Marmousi model. In comparison with dispersion effects predicted by theory, we estimate the error obtained by acoustic FWT.

## TIME-DOMAIN VISCOACOUSTIC MODELING

### Attenuation in acoustic media

The involvement of attenuation into acoustic or elastic modeling has been described by numerous authors (e. g., Carcione et al., 1988a,b; Emmerich and Korn, 1987; Blanch et al., 1995; Liu et al., 1976; Robertsson et al., 1994; Bohlen, 2002). Within the scope of this work we have developed an acoustic FWT in the time-domain. In contrast to modeling in the frequency-domain, a direct implementation of attenuation using complex velocities is not possible. Hence, the attenuative properties of the medium have to be approximated by a suitable rheology which is represented by the GSLS (Liu et al., 1976). It consists of a parallel connection of a HOOKE and $L$ MAXWELL bodies. Thus, attenuation is described by $L$ relaxation mechanisms. While an acoustic model is characterized by the parameters density $\rho$ and bulk modulus $\kappa$, the viscoacoustic medium is defined by $\rho$, the relaxed bulk modulus $\kappa_r$ and additional $2L$ relaxation parameters $\tau_{\sigma,l}$ and $\tau_{\epsilon,l}$ ($l = \{1, \ldots, L\}$). The relaxation times $\tau_{\sigma,l}$ and retardation times $\tau_{\epsilon,l}$ are required for an appropriate approximation of the quality factor $Q_P$, which is proportional to the reciprocal of attenuation $\alpha_P$. We only consider constant-$Q_P$ models, i.e., $Q_P(f) = const. = Q_{P,0}$, within the desired frequency range $f_{\min} \leq f \leq f_{\max}$ of the seismic waveforms. The general frequency-dependent relation of $Q_P(\omega)$

(with $\omega = 2\pi f$) and relaxation parameters is given by

$$Q_P(\omega, \tau_{\sigma,l}, \tau_P) = \frac{1 + \sum_{l=1}^{L} \frac{\omega^2 \tau_{\sigma,l}^2}{1+\omega^2 \tau_{\sigma,l}^2} \tau_P}{\sum_{l=1}^{L} \frac{\omega\, \tau_{\sigma,l}}{1+\omega^2 \tau_{\sigma,l}^2} \tau_P} \tag{1}$$

with the substitution (Blanch et al. (1995)

$$\tau_P := \frac{\tau_{\epsilon,l}}{\tau_{\sigma,l}} - 1 \quad \text{with} \quad \tau_P \approx \frac{2}{Q_{P,0}}. \tag{2}$$

To achieve an approximation of $Q_P(\omega) = const. = Q_{P,0}$ the nonlinear equation (1) has to be minimized by application of a least squares optimization algorithm (Blanch et al., 1995; Bohlen, 1998). Hence, the constant-$Q_P$ model is defined by $L$ relaxation times and $Q_{P,0}$. Instead of defining relaxation times, the choice of relaxation frequencies $f_{r,l} = \frac{1}{2\pi\tau_{\sigma,l}}$ for each mechanism of the GSLS is more common. Furthermore, the relaxation parameters are used to compute relaxed frequency-depended bulk modulus $\kappa_r$ and relaxed P-wave phase velocity $v_P$, respectively:

$$\kappa_r = \rho\, v_{P,0}^2 \left(1 + \sum_{l=1}^{L} \frac{\omega_0^2 \tau_{\sigma,l}^2}{1 + \omega_0^2 \tau_{\sigma,l}^2} \tau_P\right)^{-1} \quad \text{for} \quad Q_P \gg 1 \tag{3}$$

with the angular reference frequency $\omega_0 = 2\pi f_0$. At reference frequency $\omega_0$ reference velocity $v_{P,0}$ is defined, i.e., $v_{P,0}$ corresponds to the acoustic phase velocity. A useful choice of $f_0$ can be the peak frequency of the source wavelet.

**Time-domain wave equation**

In addition to relaxation of the model parameter, attenuation has to be implemented into the wave equation. The basic homogeneous second order acoustic wave equation is given by

$$\frac{1}{\rho\,(\vec{x})\, v_P^2\,(\vec{x})} \partial_t^2 p\,(\vec{x}, t) = \nabla \cdot \left(\frac{1}{\rho\,(\vec{x})} \nabla p\,(\vec{x}, t)\right) \tag{4}$$

with the pressure field $p\,(\vec{x}, t)$ at time $t$ and position $\vec{x}$. Due to the requirement of first order partial differential equations for implementation of attenuation, equation (4) has to be rewritten:

$$\begin{aligned} \partial_t\, p\,(\vec{x}, t) &= \kappa\,(\vec{x})\ \nabla \cdot \vec{w}\,(\vec{x}, t)\,, \\ \partial_t\, \vec{w}\,(\vec{x}, t) &= \frac{1}{\rho\,(\vec{x})} \nabla p\,(\vec{x}, t)\,. \end{aligned} \tag{5}$$

Vector $\vec{w}\,(\vec{x}, t)$ denotes the particle velocity field. The introduction of attenuation yields following wave equation (Emmerich and Korn, 1987; Carcione et al., 1988a; Robertsson et al., 1994):

$$\begin{aligned} \partial_t\, p\,(\vec{x}, t) &= \kappa_r\,(\vec{x})\ \nabla \cdot \vec{w}\,(\vec{x}, t)\ \left[1 + \sum_{l=1}^{L} \left(\frac{\tau_{\epsilon,l}}{\tau_{\sigma,l}} - 1\right)\right] + \sum_{l=1}^{L} r_l\,(\vec{x}, t)\,, \\ \partial_t\, r_l\,(\vec{x}, t) &= -\frac{1}{\tau_{\sigma,l}} \left[\kappa_r \left(\frac{\tau_{\epsilon,l}}{\tau_{\sigma,l}} - 1\right)\ \nabla \cdot \vec{w}\,(\vec{x}, t) + r_l\,(\vec{x}, t)\right] \quad \text{with} \quad l = \{1, \ldots, L\}, \\ \partial_t\, \vec{w}\,(\vec{x}, t) &= \frac{1}{\rho\,(\vec{x})} \nabla p\,(\vec{x}, t)\,. \end{aligned} \tag{6}$$

With substitutions based on relation (2) we get

$$\begin{aligned} \partial_t\, p\,(\vec{x}, t) &= \kappa_r\,(\vec{x})\ \nabla \cdot \vec{w}\,(\vec{x}, t)\ [1 + L\, \tau_P\,(\vec{x})] + \sum_{l=1}^{L} r_l\,(\vec{x}, t)\,, \\ \partial_t\, r_l\,(\vec{x}, t) &= -\frac{1}{\tau_{\sigma,l}} \left[\kappa_r\, \tau_P\,(\vec{x})\ \nabla \cdot \vec{w}\,(\vec{x}, t) + r_l\,(\vec{x}, t)\right] \quad \text{with} \quad l = \{1, \ldots, L\}, \\ \partial_t\, \vec{w}\,(\vec{x}, t) &= \frac{1}{\rho\,(\vec{x})} \nabla p\,(\vec{x}, t)\,. \end{aligned} \tag{7}$$

Viscoacoustic modeling in the time-domain needs additional $L$ wavefield variables $r_l(\vec{x},t)$ and $L$ equations. The so-called "memory variables" $r_l(\vec{x},t)$ characterize the memory of the viscoacoustic medium. The full waveform tomography requires the solution of the acoustic wave equation which is realized by a time-domain finite-difference time-stepping method (Alford et al., 1974) with perfectly matched layer boundary condition (cp. Berenger, 1994; Chew and Weedon, 1994) and heavy parallelization (Bohlen, 2002; Kurzmann et al., 2009). Due to time-domain modeling, attenuation is implemented by the relaxation mechanisms of the generalized standard linear solid (cp. Liu et al., 1976; Bohlen, 1998) for finite-difference implementation).

**Verification of viscoacoustic finite-difference modeling results**

In this section we employ 2D time-domain acoustic as well as viscoacoustic modeling to a homogeneous full-space example. The results are compared with an analytical solution. The model and its parameters are shown in Figure 1. For finite-difference modeling we use a grid size of $1000 \times 1600$ grid points with a spacing of $DH = 0.5$ m, a time step of $DT = 10^{-4}$ s and a Ricker wavelet with a peak source frequency of $f_s = 80$ Hz. To suppress artificial reflections from model boundaries, the acquisition geometry is surrounded by a broad perfectly matched layer (PML).
In the following time-domain viscoacoustic approach the attenuation of a medium is approximated by $L = 3$ relaxation mechanisms within the desired frequency range of $f = [0,\ 200]$ Hz, which corresponds to the relevant frequency content of the source wavelet. $L$ relaxation frequencies $f_{r,l}$ ($l = \{1,\dots,L\}$) are estimated from $Q_{P,0}$ and the reference frequency $f_0 = f_s$. This is realized by the $Q_P$-approximation method mentioned above. The result of this optimization is a logarithmically spaced set $f_{r,l} = (1.470, 21.40, 199.6)$ Hz. The approximation of the quality factor $Q_P(f)$ and the resulting dispersion $v(f)$ is illustrated by Figures 2 (a) and (b). At frequency $f_0$ we assume the acoustic reference phase velocity $v(f_0) = v_{P,0} = 2400\ \frac{\mathrm{m}}{\mathrm{s}}$. Thus, $v(f)$ ranges from $v_{\min} = v(f=0) \approx 2163\ \frac{\mathrm{m}}{\mathrm{s}}$ to $v_{\max} = v(f \to \infty) \approx 2499\ \frac{\mathrm{m}}{\mathrm{s}}$, whereas in finite-difference modeling $v(f \to \infty)$ is computed at the maximum NYQUIST frequency $f_{Ny} = 1/(2\,DT) = 5000$ Hz (with respect to time step $DT$). Both $v_{\min}$ and $v_{\max}$ have to be considered to avoid grid dispersion or instability. Hence, in forward modeling minimum and maximum velocities are computed as follows:

$$v_{\min} = v_{P,0}\sqrt{\frac{1}{1+\sum_{l=1}^{L}\frac{\omega_0^2\tau_{\sigma,l}^2}{1+\omega_0^2\tau_{\sigma,l}^2}\tau_P}} \quad \text{and} \quad v_{\max} = v_{P,0}\sqrt{\frac{1+L\,\tau_P}{1+\sum_{l=1}^{L}\frac{\omega_0^2\tau_{\sigma,l}^2}{1+\omega_0^2\tau_{\sigma,l}^2}\tau_P}}. \tag{8}$$

In case of the homogeneous model experiment equations (8) yield velocities $v_{\min} \approx 2184\ \frac{\mathrm{m}}{\mathrm{s}}$ and $v_{\max} \approx 2491\ \frac{\mathrm{m}}{\mathrm{s}}$, which slightly differ from the theoretical values.
The effect of attenuation on seismic data is demonstrated by a comparison of acoustic and viscoacoustic modeling based on the given acquisition geometry. Figure 3 shows the resulting seismograms. As expected with increasing offset a significant amplitude decay and a modification of phases can be observed. Especially the amplitudes of high frequency contents are subject to strong attenuation (cp. amplitude spectrum in Figure 4(a)). Furthermore, Figure 4(b) visualizes a comparison of acoustic and viscoacoustic phase spectra. The frequency-dependent phase distortions mainly occurr at frequencies $f > f_0$ and disappear around the peak frequency.
Hereafter we verify the results of viscoacoustic finite-difference modeling using the program *AnalyticAnelastic* (implemented by JOSEP DE LA PUENTE, LMU Geophysics, Munich; based on (Carcione et al., 1988b; Carcione, 2001; Emmerich and Korn, 1987). It provides the same rheology as mentioned above and is utilized for computation of a semi-analytical solution of the wave equation in a viscoelastic and consequently viscoacoustic or acoustic medium. Figure 5(a) shows the acoustic reference comparison for an exemplary trace at farest offset ($x = 340$ m). Both semi-analytical and finite-difference solution fit very well. The viscoacoustic data at near offset ($x = 20$ m) and far offset ($x = 340$ m) are depicted in Figures 5(b) and 5(c). Apart from minor deviations, the finite-difference solution resembles the analytical solution.

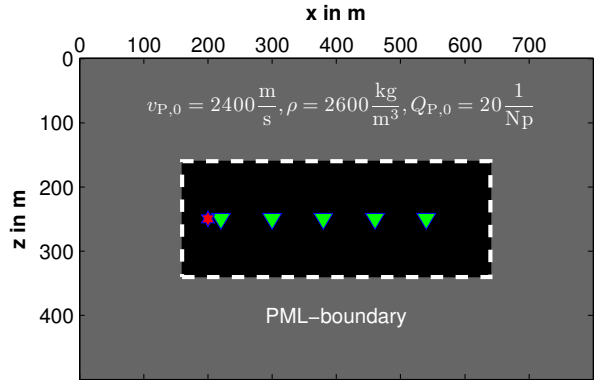


**Figure 1:** Viscoacoustic homogeneous full-space model used for time-domain finite-difference modeling. The acquisition geometry consists of one directed force source in vertical direction (red star) and five receivers (green triangles).

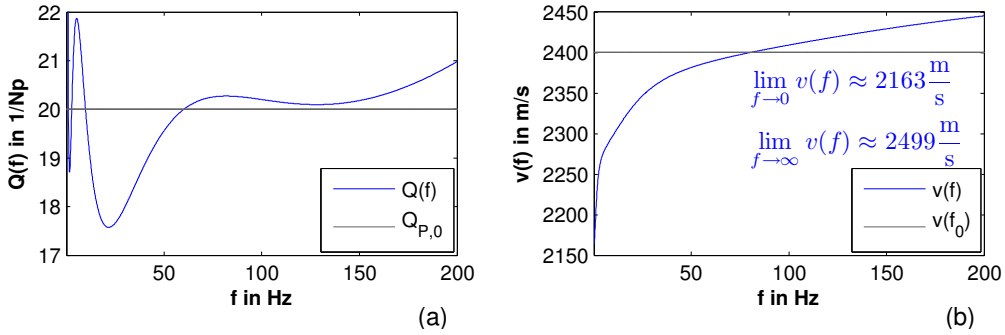


**Figure 2:** Figure a): Approximation of the quality factor $Q_P(f, L = 3)$ for the model shown in Figure 1 and the desired frequency range of the underlying source signal. Figure b): Corresponding dispersion curve based on an acoustic reference velocity model $v(f_0) = v_{P,0} = 2400\ \frac{m}{s}$.

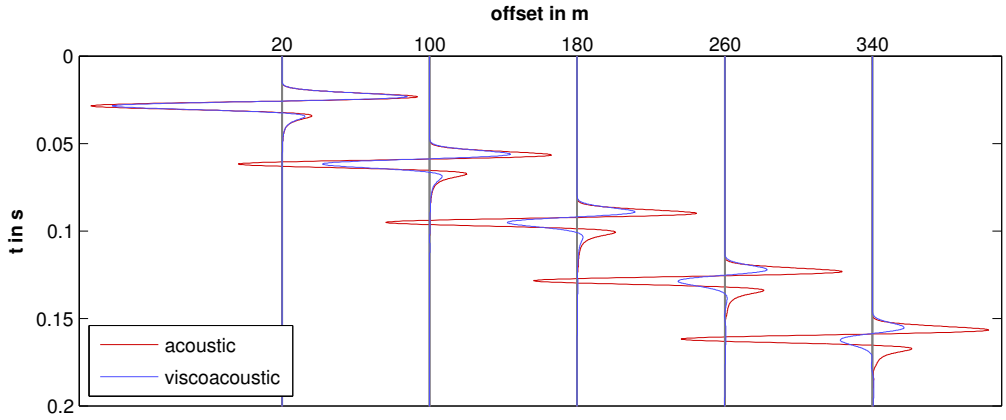


**Figure 3:** Seismogram corresponding to the acquisition geometry in Figure 1. The data represent the vertical component of particle velocities. Due to plotting issues, all traces are normalized to maximum amplitude of the acoustic signals.

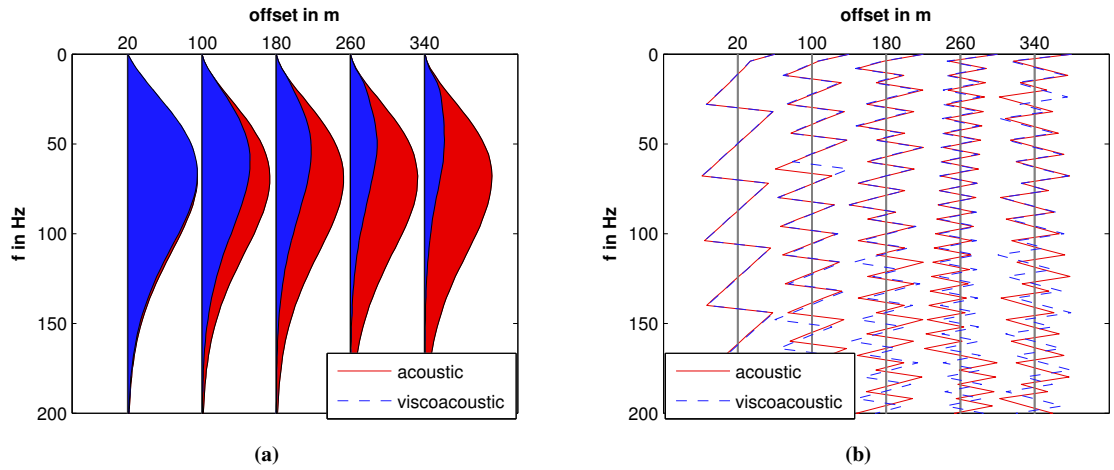


**Figure 4:** Amplitude (Figure (a)) and phase spectra (Figure (b)) of the seismic data shown in Figure 3. All traces in Figure (a) are normalized to maximum values of the acoustic spectra.

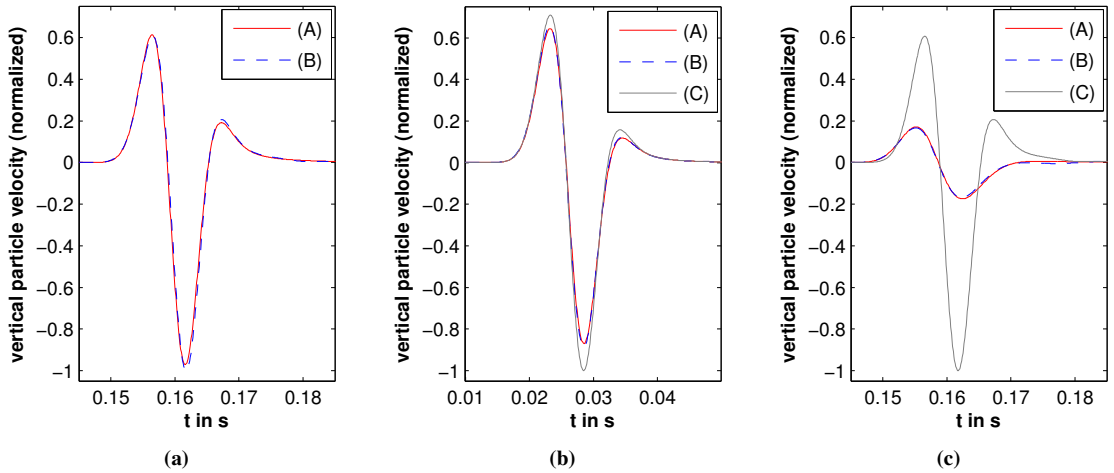


**Figure 5:** Comparison of semi-analytical and finite-difference solutions. Exemplary data is shown for the acoustic case at far offset (Figure (a)), for viscoacoustic data at near offset (Figure (b)) and far offset (Figure (c)). Traces (A) are represented by the analytical solution, traces (B) by finite-difference solution and traces (C) by the corresponding acoustic solution in Figure (a).

## SYNTHETIC FULL WAVEFORM TOMOGRAPHY EXPERIMENTS

In the following we investigate the impact of attenuation on acoustic FWT. Depending on the aim of this work some restrictions are applied:

- the FWT only inverts for P-wave velocity model $v_P$,
- to focus on attenuation effects the density model is neglected,
- initial source signal $s_0 = s_{\text{true}}$,
- progress and result of FWT are tested for both the absence of attenuation and an initial quality factor model $Q_P$ which will be used as passive model parameter,
- in the following 1D and 2D examples FWT is not allowed to apply model updates within the water

layer due to the assumption of known parameters $v_P = 1500\ \frac{\mathrm{m}}{\mathrm{s}}$ and $Q_P = 60000\ \frac{1}{\mathrm{Np}}$ (minimum value for salt water at frequency which is much higher than seismic frequencies, cp. Johnston, 1981),

- the algorithm comprises gradient computation based on the $L^2$ misfit function and the conjugate gradient method (Mora, 1987),
- to avoid unwanted side effects, only a minimum repertoire of preconditioning features is applied: time-wondowing of the data is omitted, low-pass filtering of observed data over multiple stages [Bunks et al. (1995) and analogous to frequency selection in frequency-domain FWT (Sirgue and Pratt, 2004)] is applied in case of Marmousi model, wavefield-based preconditioning (Fichtner et al., 2009; Igel et al., 1996) of the gradient is performed for both 1D and 2D model.

**Synthetic experiment 1: 1D model**

The first example consists of a layered 1D model with a water layer on top, followed by low and high attenuative sedimentary rocks (Figure 6). It represents an extreme case of subsurface properties within a marine environment, i.e., the placement of a highly attenuative layer at top of sedimentary rocks. The acquisition geometry is located at the free surface and consists of 24 explosive sources as well as 278 hydrophones (for each source all receivers are used). The source signal consists of a Ricker wavelet with a peak frequency $f_s = 80$ Hz. The model size is $130 \times 308$ m which results – using a grid spacing $DH = 0.5$ m – in a grid size of $260 \times 616$ grid points. Due to the application of a perfectly matched layer (width = 15 m) for avoiding artificial boundary reflections in finite-difference modeling, all model related figures are limited to the illustration of the relevant area. Furthermore, the synthetic seismic data is obtained by application of a record time of 0.21 s with a time discretization of $DT = 8 \cdot 10^{-5}$ s.
The approximation of relaxation parameters are based on reference frequency $f_0 = f_s$ and an average $\bar{Q}_P = 74\ \frac{1}{\mathrm{Np}}$ within the area from layer two to layer five. Using three relaxation mechanisms we get the relaxation frequencies $f_{r,l} = (1.196, 17.58, 179.1)$ Hz. Both the acoustic and viscoacoustic data are shown for a central shot (Figure 7). Due to missing attenuation in water, phases and amplitudes of direct wave and even the seafloor reflection match very well. However all later reflection events of the acoustic data are characterized by phase distortions and a significant amplitude decay. The phase misfit is explained by the high dispersive properties of layer two. The dispersion contributions of all layers are computed by equations (8). The resulting minimum and maximum frequency-dependent velocities are visualized by vertical sections across the 1D medium (Figure 8 (a)).
Regarding the 1D model several full waveform inversions have been employed to investigate the sensitivity of acoustic FWT to viscoacoustic data as well as the efficiency of FWT with viscoacoustic modeling and different initial models (cp. Table 1).

| | data | used offsets | modeling | initial model(s) |
|---|---|---|---|---|
| Reference FWT | acoustic | all | acoustic | smooth $v_P$ model |
| Test 1 | viscoacoustic | all | acoustic | smooth $v_P$ model |
| Test 2 | viscoacoustic | all | viscoacoustic | smooth $v_P$ and $Q_P$ models |
| Test 3 | viscoacoustic | all | acoustic | true $v_P$ model |
| Test 4 | viscoacoustic | near | acoustic | true $v_P$ model |

**Table 1:** 1D model: Compilation of all acoustic FWT tests.

The initial models are generated by application of a 2D Gaussian filter (size $100 \times 100$ m, $\sigma = 33$) to the sub-seafloor area of the true model (cp. Figure 8 (b) and (c)). A reliable interpretation of the effects caused by attenuation can be done by adding an acoustic reference result. The nearly optimal conformity of true and final model (Figure 8 (d)) ensures the applicability of FWT to the given model which comprises acoustic observed data and pure acoustic inversion. The vertical section of this and following inversion results is computed by lateral averaging of a representative model area which is located at $x = [80,\ 228]$ m. This avoids artificial velocity recovery due to poor ray coverage close to the lateral model boundaries.
Figure 9 opposes several FWTs applied to viscoacoustic observed data which will be discussed subse-

quently. Corresponding exemplary data plots can be found in Figure 10. All subfigures of Figure 9 contain auxiliary dispersion plots with estimated minimum and maximum velocity boundaries. Based on $v_0$, $v_{\min}$ and $v_{\max}$ from Figure 8 (a) depth-dependent one-way traveltimes of a zero-offset ray can be computed by

$$\tilde{t}_{0,\min,\max}(z) = \int_{z=0}^{\max z} \frac{dz}{v_{0,\min,\max}(z)}. \tag{9}$$

The "cumulative" dispersion effect is expressed by

$$\tilde{v}_{\min}(z) = v_0(z)\,\frac{\tilde{t}_0(z)}{\tilde{t}_{\min}(z)} \quad \text{and} \quad \tilde{v}_{\max}(z) = v_0(z)\,\frac{\tilde{t}_0(z)}{\tilde{t}_{\max}(z)}. \tag{10}$$

However, as mentioned above equations (9) and (10) apply to zero-offset ray paths only. Due to the existence of near and far offsets, they can be treated as a rough estimation for velocity dispersion.

**Test 1** deals with the application of acoustic FWT to viscoacoustic data (Figure 9 (a)). The velocity model is recovered insufficiently which is explained by a bad fit of observed and sythetic data (Figure 10 (a)).

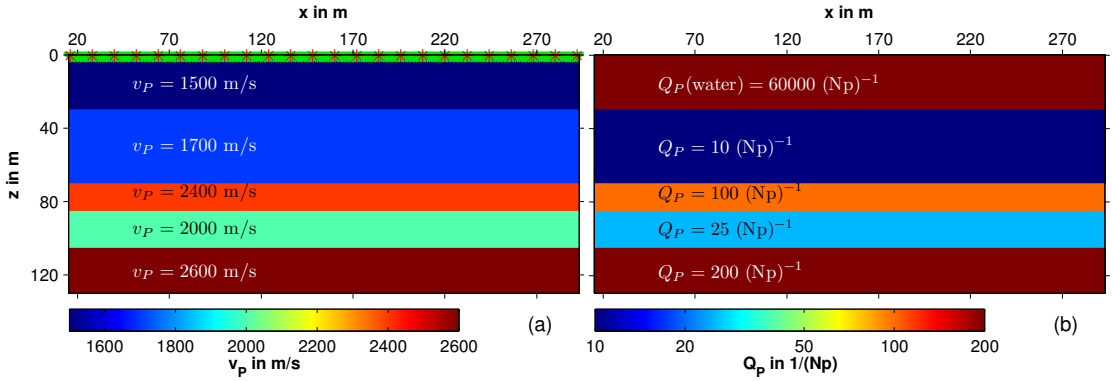


**Figure 6:** 1D model: The synthetic P-wave velocity model is shown in Figure (a) and the corresponding quality factor in Figure (b), with $Q_P(\text{water}) = 60000\ \frac{1}{\text{Np}}$. The acquisition geometry is symbolized by red (sources) and green markers (receivers).

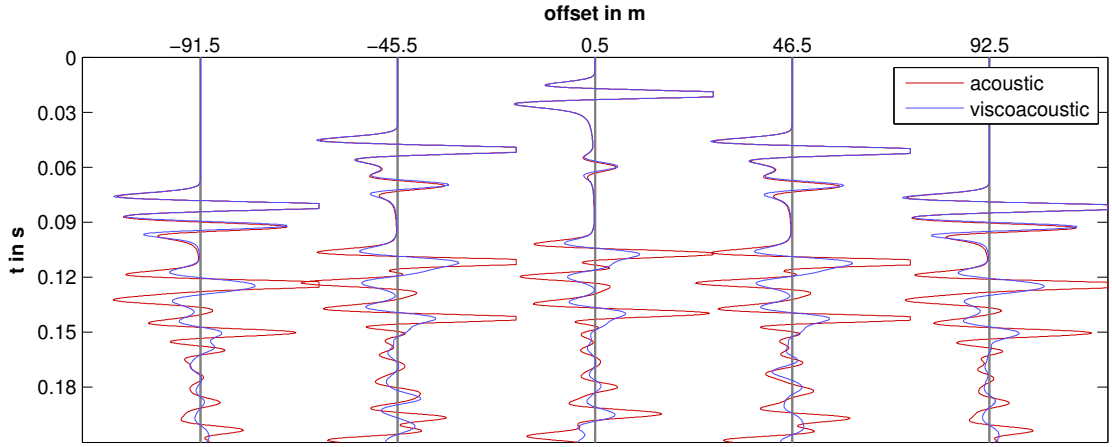


**Figure 7:** 1D model: Observed acoustic and viscoacoustic data for the central shot 13 at $x = 160$ m and with traces at representative offsets. For better visualization a gain factor of $t^2$ is applied, traces are normalized to maximum amplitude of the acoustic signals and high amplitudes are clipped.

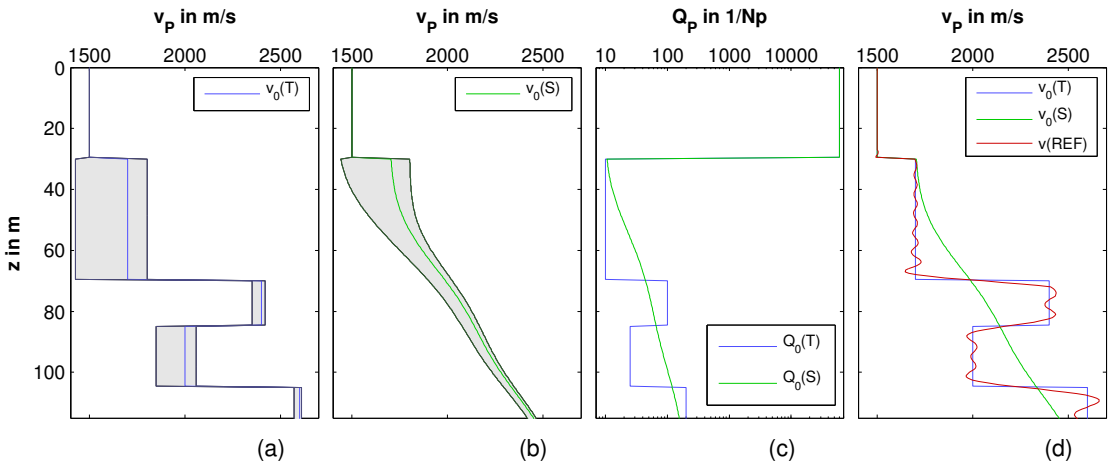


**Figure 8:** 1D model: Vertical cross sections of $v_P$ and $Q_P$ models. The abbreviations "T", "S" and "REF" refer to true model, starting model and reference result. Figure (a) shows the true $v_P$ model and its contribution to dispersion based on the true quality factor in Figure (c). The $v_P$ starting model is shown in Figure (b). Its dispersion limits (shaded areas) correspond to the initial quality factor in Figure (c). Figure (d) illustrates the reference result of a pure acoustic FWT.

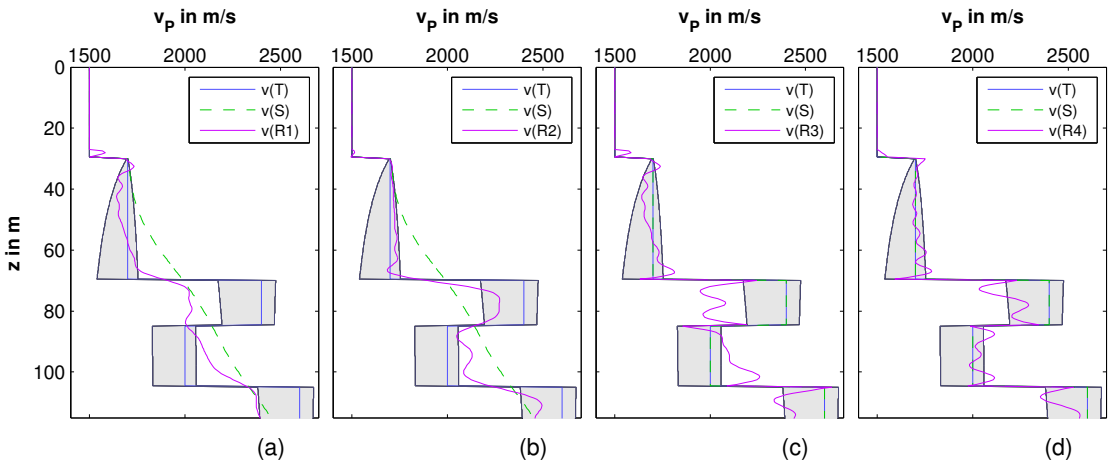


**Figure 9:** 1D model: Compilation of several FWT results for the 1D medium. Additionally to Figure 8, the abbreviations "R1"…"R4" represent the resulting velocity models. The subfigures (a), (c) and (d) show the application of acoustic FWT to viscoacoustic data for different starting models. Subfigure (b) illustrates the result of acoustic FWT with viscoacoustic modeling to viscoacoustic data. In subfigures (a), (b) and (c) data at all offsets and in subfigure (d) only near-offset data are involved. The shaded areas symbolize the "cumulative" dispersion effect.

The comparison of true and final velocity model shows an improvement, but in particular the incomplete reconstruction of layers three and four are due to wrong attenuation provided by the starting model (cp. Figures 8 (a) and (b)). The result is a smooth velocity model with an indication of interfaces.
**Test 2** includes attenuation and applies acoustic FWT to the viscoacoustic dataset (Figure 9 (b)). The initial $Q_P$-model (Figure 8 (c)) remains unchanged throughout the entire inversion. In contrast to the previous result, we can observe a siginificant improvement of the velocity model. The fit between synthetic and

observed data is much better (Figure 10 (b)).
**Test 3** investigates acoustic FWT applied to viscoacoustic data, where the true velocity model is used as starting model. In spite of using the correct $v_P$-model, the FWT tries to reduce the data misfit (cp. Figure 10 (c)) by modifying the magnitude of the velocities. The location of the interfaces seems to be unchanged. However, we can observe an exceeding of the dispersion limit assumption. The involvement of all offsets violates the applicability of equations (10). Consequently, in particular the central layer three is "smeared" heavily.
**Test 4** is a modification of the previous test. Due to the restriction of utilizing zero-offset ray paths for computation of dispersion limits, the available offsets are reduced. The FWT takes into account offsets from -20 m to 20 m at every shot position. Again the FWT tries to update the initial (= true) model, but at prevailing portion of depth locations it does not exceed the predicted dispersion limits (Figure 9 (d)).

Based on a medium containing highly attenuative structures, acoustic FWT is not able to recover the velocity model successfully from viscoacoustic data. Even if we use the true velocity model as starting model, the misfit between viscoacoustic observed data and acoustic synthetic data is mapped to the velocity model by modifying its magnitudes. However, the usage of an passive $Q_P$ model improves the velocity reconstruction tremendously.

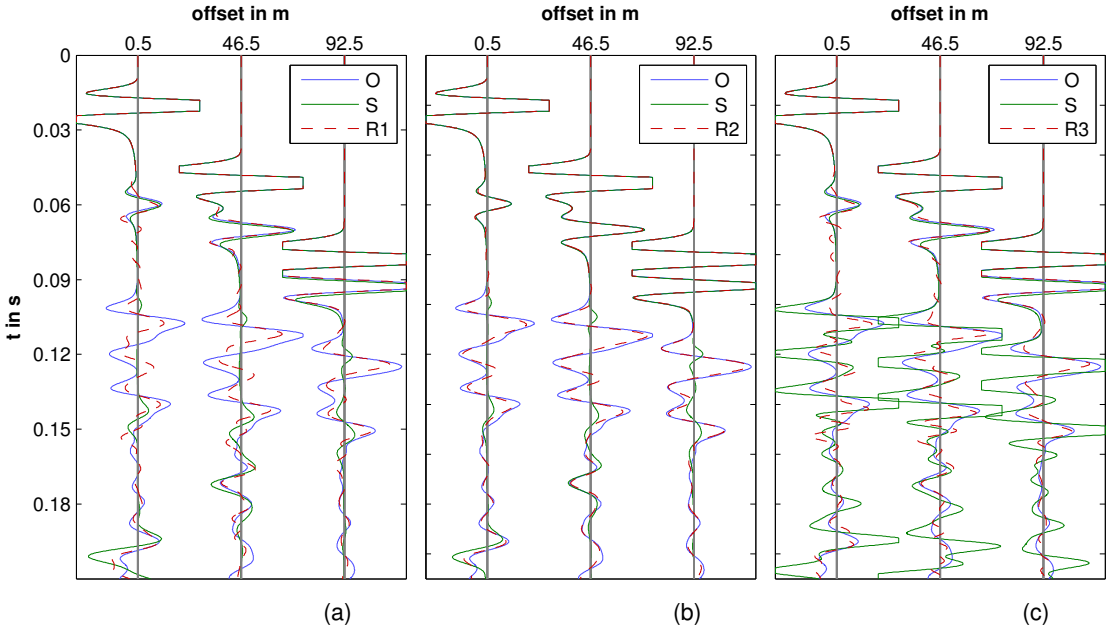


**Figure 10:** 1D model: Compilation of exemplary traces at representative offsets which refer to the results of tests 1 to 3 in Figures 9 (a), (b) and (c). The abbreviations "O", "S" and "R" stand for observed data, synthetic data of initial model and data of resulting model. In analogy to Figure 7 the same gain factor and clipping are applied to the traces. All traces are normalized to maximum amplitude of the observed waveforms.

### Synthetic experiment 2: 2D Marmousi model

In analogy to the previous section similar investigations are applied to a section of the Marmousi-2 model (Figure 11 (a)) based on Versteeg (1994) and Martin (2002). Hereby the velocities are clipped to the range $v_P = [1500, 4000]\ \frac{\mathrm{m}}{\mathrm{s}}$ to reduce computational efforts. The acquisition geometry is located at the free surface and consists of 32 explosive sources as well as 485 hydrophones. For each source data are recorded at all receivers. The source signal consists of a Ricker wavelet with a dominant frequency $f_s = 9$ Hz.

The model size is $3000 \times 10000$ m which results – using a grid spacing $DH = 5$ m – in a grid size of $600 \times 2000$ grid points. Due to the application of a perfectly matched layer (width = 150 m) for avoiding artificial boundary reflections in finite-difference modeling, all model related figures are limited to the relevant area. Furthermore, the synthetic seismic data is obtained by application of a record time of 5.145 s with a time discretization of $DT = 7 \cdot 10^{-4}$ s.
The $Q_P$ model is derived from the velocity model by the relationship for dissipation $1/Q_P$ (Hamilton, 1972)

$$\frac{1}{Q_P} = \alpha_P \frac{v_P}{\pi f - \frac{\alpha_P^2 v_P^2}{4\pi f}} \tag{11}$$

with intrinsic attenuation $\alpha_P$ for the frequency range of the given example in marine sedimentary rocks (Figure 12 (a)). The quality factor ranges from 21 $\frac{1}{\mathrm{Np}}$ in the upper sedimentary rocks to approximately 707 $\frac{1}{\mathrm{Np}}$ in deeper high velocity zones. The approximation of relaxation parameters are based on reference frequency $f_0 = f_s$ and an average $\bar{Q}_P = 62$ $\frac{1}{\mathrm{Np}}$ within the area beneath the seafloor. In case of the true model we can compute the relative minimum and maximum dispersion by

$$d_{\min} = \frac{v_{\min} - v_{P,0}}{v_{P,0}} \quad \text{and} \quad d_{\max} = \frac{v_{\max} - v_{P,0}}{v_{P,0}}, \tag{12}$$

which is depicted in (Figure 13). Both the acoustic and viscoacoustic data are shown for the central shot 17 (Figure 14). Using three relaxation mechanisms we get the relaxation frequencies $f_{r,l} = (0.1513, 1.925, 18.94)$ Hz. Regarding the Marmousi model three full waveform inversions have been applied to investigate the sensitivity of acoustic FWT to viscoacoustic data as well as the efficiency of FWT with viscoacoustic modeling. The initial models are generated by application of a 2D Gaussian filter (size $1250 \times 1250$ m, $\sigma = 51$) to the sub-seafloor area of the true model (cp. Figure 11 (b) and Figure 12 (b)). Again a pure acoustic inversion of acoustic data is used as reference result (Figure 11 (c)). All FWTs are divided into multiple stages to reduce nonlinearity of the inverse problem. By application of low-pass filters the inversion is performed for different frequency ranges, moving fom low to high frequencies (Sirgue and Pratt, 2004). In the following, the results are presented in conjunction with the deviation from this optimal acoustic result (tests 1 and 2) as well as with the deviation from the true model (test 3).

**Test 1** applies acoustic FWT to the viscoacoustic data. The final result shows a poor reconstruction of the velocity model (Figure 15 (a)). The model deviation in Figure 15 (b) exemplifies the FWT's inability to recover structures with high velocity contrasts. In analogy to the 1D example the model resolution decreases dramatically with increasing depth.
**Test 2** demonstrates the application of acoustic FWT with viscoacoustic modeling, whereas the initial $Q_P$ model (Figure 12 (b)) remains unchanged. In contrast to Figure 15, the entire final model shows significant improvements. However, due to the smoothness of the initial $Q_P$ model, it is impossible to recover high contrasts.
**Test 3** resembles its counterpart in the previous section. The true velocity model is used as initial model. The acoustic FWT tries to find a model which explains the misfit between acoustic and viscoacoustic data. Hence, we can observe a smoothing effect and artificial structures (Figure 17). Any further progress will "damage" the model continuously.

Obviously, in all tests the theoretical dispersion (Figure 13) is exceeded significantly by the relative model deviations. In analogy to the 1D example, the theoretical values can be treated as contributions to dispersion at each location of the subsurface. Hence, the overall "dispersive" effect is much higher.

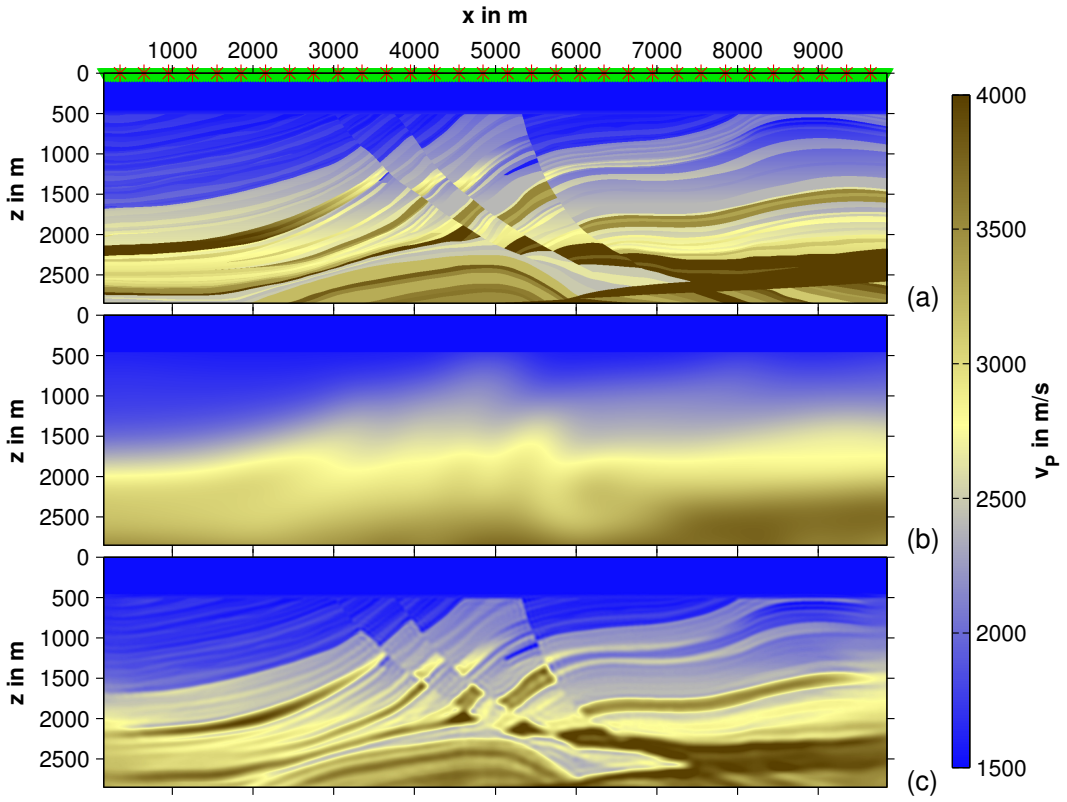


**Figure 11:** 2D model: Synthetic Marmousi velocity model. The real P-wave velocity model is shown in Figure (a), the corresponding initial model for FWT in Figure (b) and the reference result of pure acoustic FWT in Figure (c). The acquisition geometry is symbolized by red (sources) and green markers (receivers).

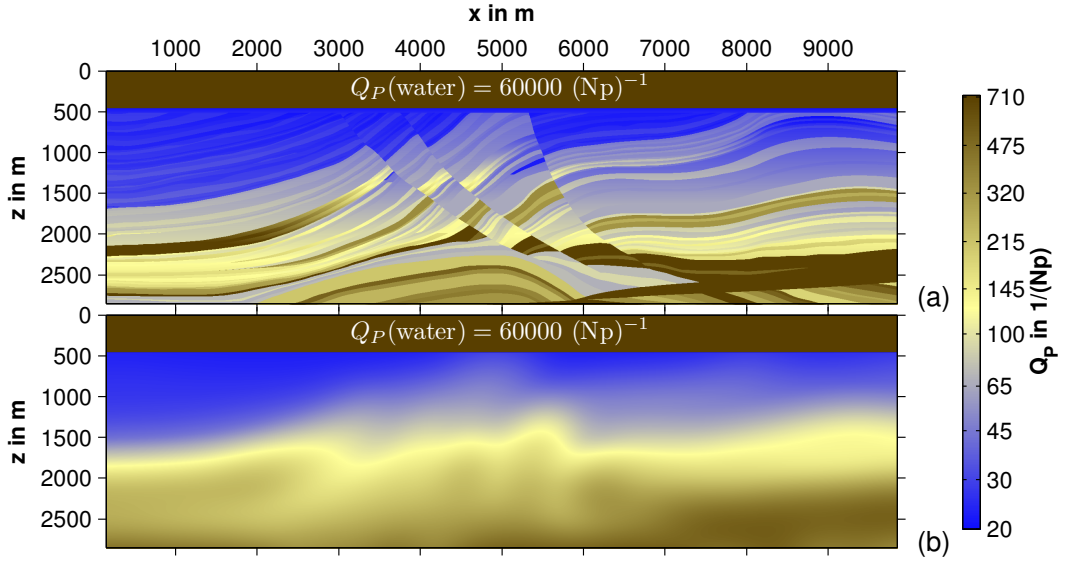


**Figure 12:** 2D model: Synthetic Marmousi $Q_P$ model. The real quality factor is shown in Figure (a) and the corresponding initial model for FWT in Figure (b).

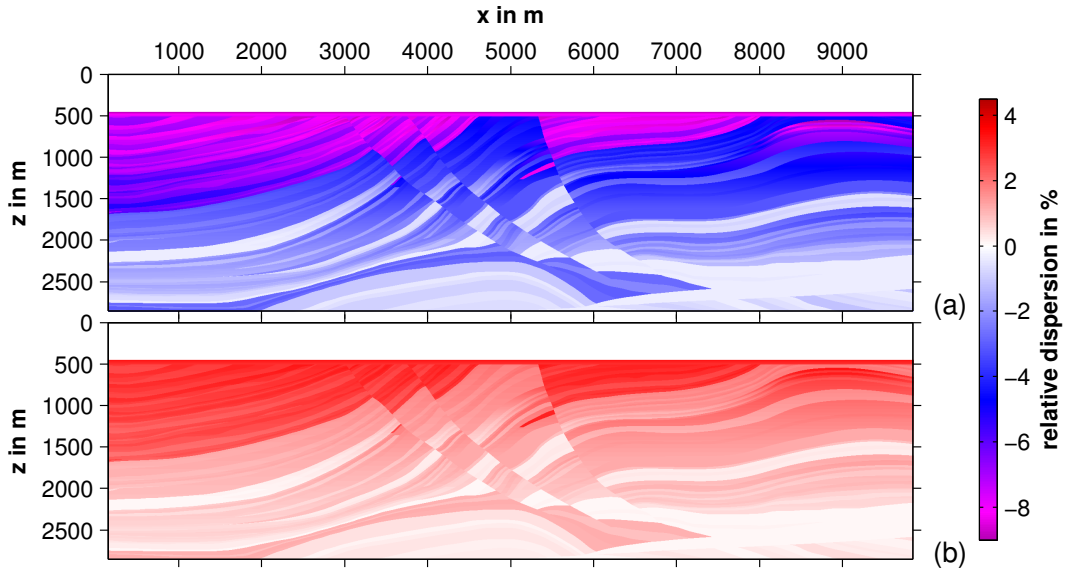


**Figure 13:** 2D model: Theoretical minimum (Figure (a)) and maximum (Figure (b)) velocity dispersion with respect to the acoustic reference velocity $v_0$ ($f_0$) at reference frequency $f_0$ (cp. equations (8) and (12).

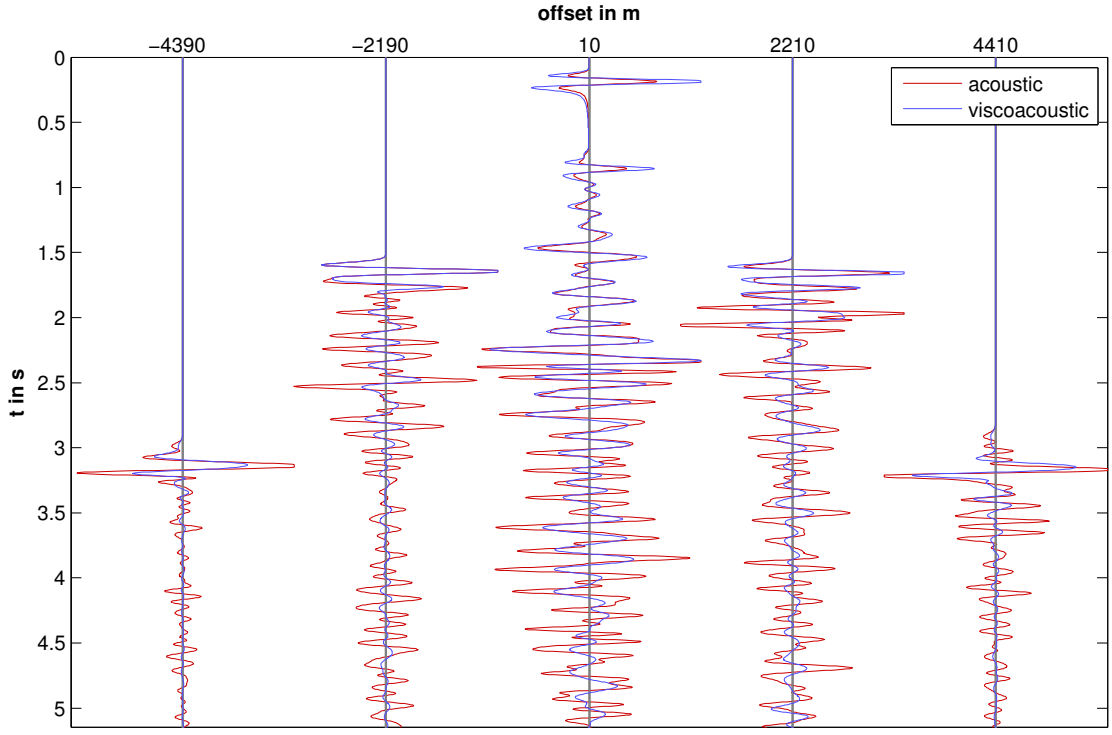


**Figure 14:** 2D model: Composition of exemplary acoustic and viscoacoustic traces of the dataset obtained at the central shot position 17 ($x = 5150$ m) related to the real Marmousi model in Figures 11 (a) and 12 (a). Due to visualization reasons, traces are normalized, partly clipped and modified by a gain factor of $t^2$. All traces are normalized to maximum amplitude of the acoustic waveforms.

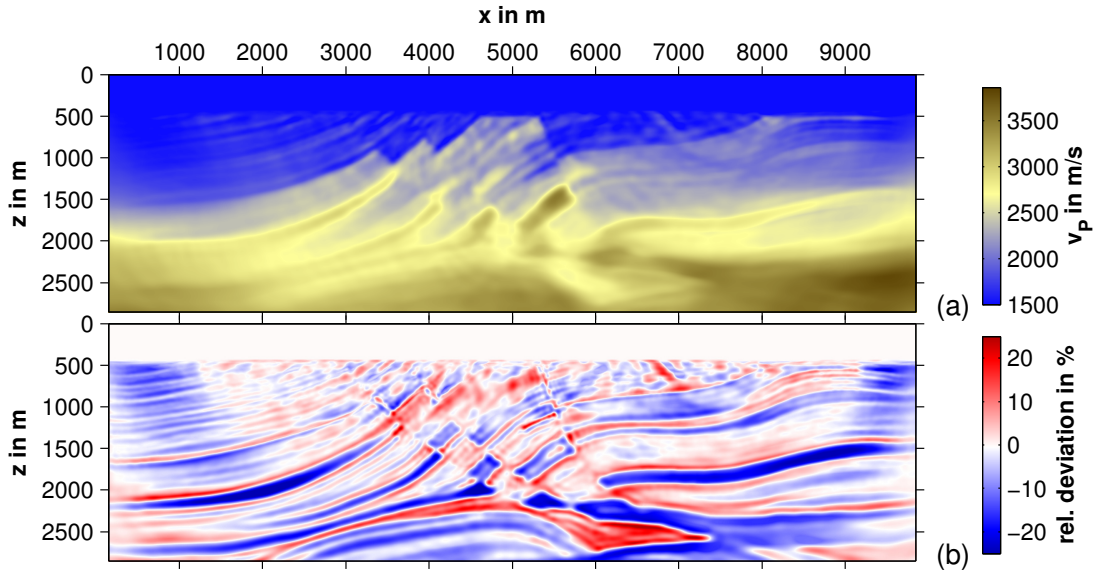


**Figure 15:** 2D model: Resulting $v_P$ model for an application of acoustic FWT to viscoacoustic data (Figure (a)) and its relative deviation (Figure (b)) from the optimal acoustic result in Figure 11 (c). The range of deviation is $[-30,\ 29]$ percent with an average absolute error of 5.7 percent within the sub-seafloor area. The image data is clipped at $\pm$ 25 percent.

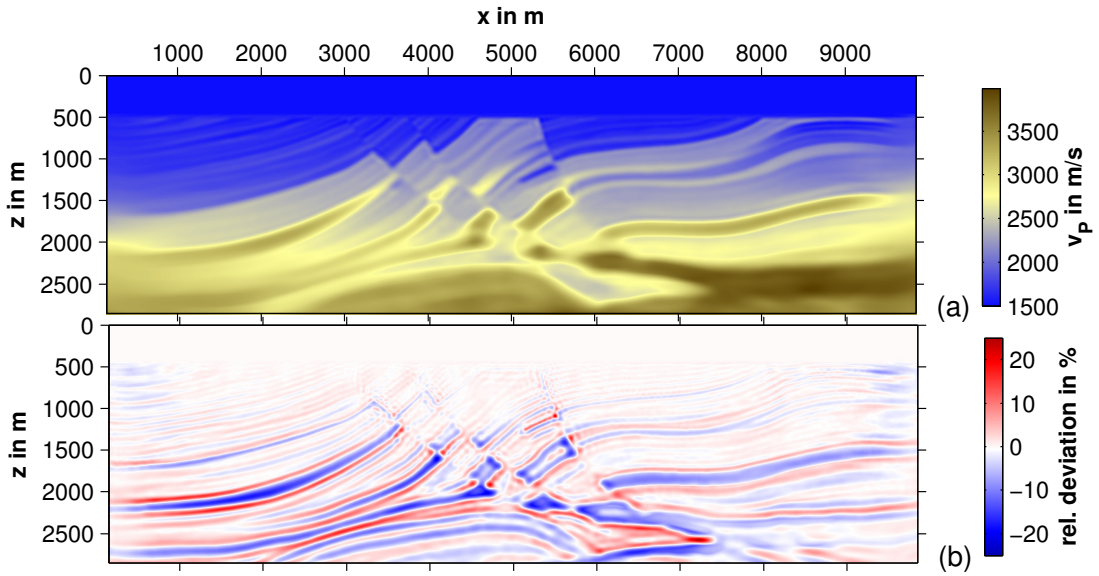


**Figure 16:** 2D model: Resulting $v_P$ model for an application of acoustic FWT with viscoacoustic modeling (using the initial $Q_P$ model in Figure 12 (b)) to viscoacoustic data (Figure (a)) and its relative deviation (Figure (b)) from the optimal acoustic result in Figure 11 (c). The range of deviation is $[-21,\ 24]$ percent with an average absolute error of 2.5 percent within the sub-seafloor area.

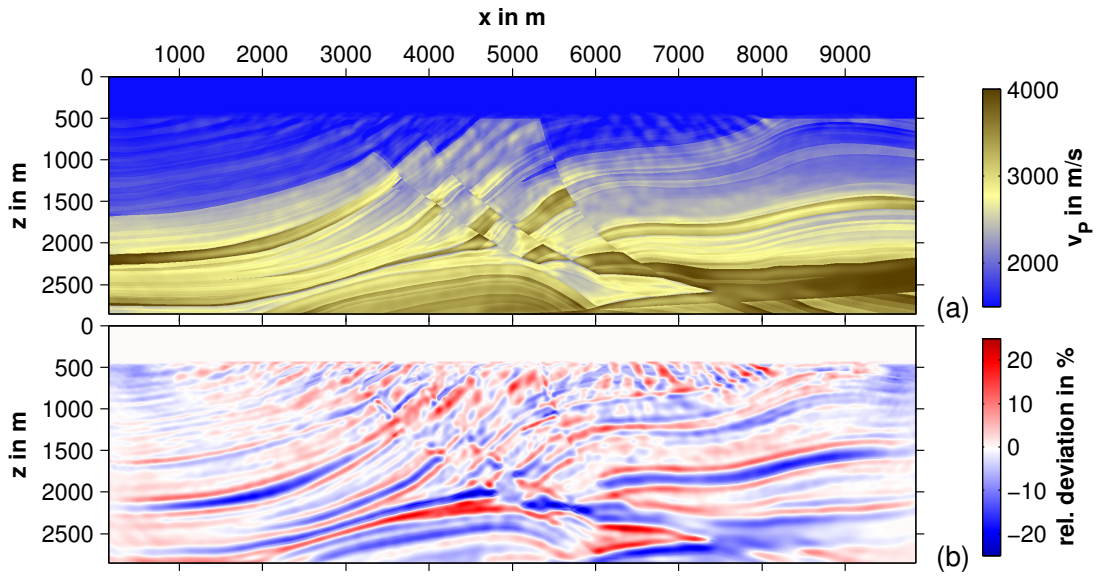


**Figure 17:** 2D model: Resulting $v_P$ model for an application of acoustic FWT (using the true $v_P$ model as starting model) to viscoacoustic data (Figure (a)) and its relative deviation (Figure (b)) from the true $v_P$ model. The range of deviation is $[-24,\ 23]$ percent with an average absolute error of 3.9 percent within the sub-seafloor area.

## CONCLUSIONS

In this work we have implemented attenuation into time-domain modeling of 2D acoustic full waveform tomography by utilizing relaxation mechanisms of the generalized standard linear solid. Using a homogeneous full-space our viscoacoustic finite-difference solution coincides with a semi-analytical solution.
Acoustic FWT has been applied to viscoacoustic data for both a model with a 1D structure and the 2D Marmousi model. Despite of using good starting models, the FWT is unable to recover the real velocity model as well as to fit the observed data properly. Hence, the misfit between acoustic and viscoacoustic data cannot be explained by acoustic FWT. In comparison with the pure acoustic reference result the acoustic reconstruction of the Marmousi model yields an inacceptable absolute model error up to 30 percent. An improvement can be obtained by involving attenuation as a passive parameter in modeling. The quality factor is estimated from $v_P$ by using a common relationship for marine sediments. On the condition of the validity of this relationship within the entire subsurface, we get a proper $Q_P$ model. Otherwise imprecise rock properties will affect the inverted $v_P$ model negatively. Compared to the neglection of attenuation, the inversion results are enhanced significantly by using a smooth initial $Q_P$ model, which was derived from the true model. However, because of its difficult estimation in field data application, an inappropriate $Q_P$ model might cause an insufficient inversion result.
Additionally, acoustic FWT with true velocity as starting model gives an impressive illustration of the attenuation's impact on the inverted velocity model. For example, in case of the Marmousi model the FWT tries to explain the misfit between acoustic and viscoacoustic data by a model "correction" up to 24 percent. Due to shorter ray paths across the 1D medium, another test with restriction to inversion of near-offset data only yields an improved resulting velocity model and reproduces the predicted dispersive effects quite well. However, the latter limitation contradicts the common assumption of using both near- and far-offset data to recover the velocity model successfully.
We conclude that at least a passive involvement of attenuation into acoustic FWT is recommended to improve the reconstruction of velocity models. However, in this case the FWT is not able to explain the remaining data misfit introduced by the fixed attenuation model assumption. Preconditioning methods have to be investigated to mitigate that problem.

## ACKNOWLEDGMENTS

This work was kindly supported by the sponsors of the *Wave Inversion Technology (WIT) Consortium*. Furthermore, we are grateful for using the supercomputers *JUROPA* at Jülich Supercomputing Centre and *HP XC3000* at Steinbuch Centre for Computing (KIT, Karlsruhe).

## REFERENCES

Alford, R. M., Kelly, K. R., and Boore, D. M. (1974). Accuracy of finite-difference modeling of the acoustic wave equation. *Geophysics*, 39(6):834–842.

Berenger, J. P. (1994). A Perfectly Matched Layer for the Absorption of Electromagnetic Waves. *Journal of Computational Physics*, 114:185–200.

Blanch, J. O., Robertsson, J. O. A., and Symes, W. W. (1995). Modeling of a constant q: Methodology and algorithm for an efficient and optimally inexpensive viscoelastic technique. *Geophysics*, 60(1):176–184.

Bohlen, T. (1998). *Viskoelastische FD-Modellierung seismischer Wellen zur Interpretation gemessener Seismogramme*. PhD thesis, Christian-Albrechts-Universität zu Kiel.

Bohlen, T. (2002). Parallel 3D viscoelastic finite difference seismic modelling. *Computers and Geosciences*, 28:887–899.

Brenders, A. J. and Pratt, R. G. (2007). Full waveform tomography for lithospheric imaging: results from a blind test in a realistic crustal model. *Geophysical Journal International*, 168(1):133–151.

Bunks, C., Saleck, F. M., Zaleski, S., and Chavent, G. (1995). Multiscale seismic waveform inversion. *Geophysics*, 60(5):1457–1473.

Carcione, J. M. (2001). *Wave fields in real media; wave propagation in anisotropic, anelastic and porous media*. Amsterdam; New York: Pergamon.

Carcione, J. M., Kosloff, D., and Kosloff, R. (1988a). Wave propagation simulation in a linear viscoacoustic medium. *Geophysical Journal of the Royal Astronomical Society*, 93(2):393–407.

Carcione, J. M., Kosloff, D., and Kosloff, R. (1988b). Wave propagation simulation in a linear viscoelastic medium. *Geophysical Journal of the Royal Astronomical Society*, 95(3):597–611.

Chew, W. C. and Weedon, W. H. (1994). A 3D perfectly matched medium from modified Maxwell's equations with stretched coordinates. *Microwave and Optical Technical Letters*, 7(13):599–604.

Emmerich, H. and Korn, M. (1987). Incorporation of attenuation into time-domain computations of seismic wave fields. *Geophysics*, 52(9):1252–1264.

Fichtner, A., Kennett, B. L. N., Igel, H., and Bunge, H. (2009). Full seismic waveform tomography for upper-mantle structure in the Australasian region using adjoint methods. *Geophysical Journal International*, 179:1703–1725.

Hak, B. and Mulder, W. (2008). Preconditioning for linearized inversion of attenuation and velocity perturbations. In *Expanded abstracts, 78th Annual International Meeting*, pages 2036–2040. SEG.

Hak, B. and Mulder, W. A. (2011). Seismic attenuation imaging with causality. *Geophysical Journal International*, 184:439–451.

Hamilton, E. L. (1972). Compressional-wave attenuation in marine sediments. *Geophysics*, 37(4):620–646.

Hicks, G. J. and Pratt, R. G. (2001). Reflection waveform inversion using local descent methods: estimating attenuation and velocity over a gas-sand deposit. *Geophysics*, 66(2):598–612.

Igel, H., Djikpéssé, H., and Tarantola, A. (1996). Waveform inversion of marine reflection seismograms for P impedance and Poisson's ratio. *Geophysical Journal International*, 124:363–371.

Johnston, D. H. (1981). Attenuation: A state-of-art summary. In Toksöz, M. N. and Johnston, D. H., editors, *Seismic Wave attenuation*. Geophysics reprint series, no. 2: Society of Exploration Geophysicists.

Kamei, R. and Pratt, R. G. (2008). Waveform tomography strategies for imaging attenuation structure for cross-hole data. In *Extended Abstracts, 70th Conference and Technical Exhibition*. EAGE. F019.

Kurzmann, A., Köhn, D., Przebindowska, A., Nguyen, N., and Bohlen, T. (2009). 2D Acoustic Full Waveform Tomography: Performance and Optimization. In *Extended Abstracts, 71st Conference and Technical Exhibition*. EAGE.

Liu, H. P., Anderson, D. L., and Kanamori, H. (1976). Velocity dispersion due to anelasticity: implications for seismology and mantle composition. *Geophysical Journal of the Royal Astronomical Society*, 47(1):41–58.

Malinowski, M., Operto, S., and Ribodetti, A. (2011). High-resolution seismic attenuation imaging from wide-aperture onshore data by visco-acoustic frequency-domain full-waveform inversion. *Geophysical Journal International*, 186:1179–1204.

Martin, G. (2002). Marmousi-2: An updated model for the investigation of AVO in structurally complex areas. In *Expanded abstracts, 72nd Annual International Meeting*. SEG.

Mora, P. (1987). Nonlinear two-dimensional elastic inversion of multioffset data. *Geophysics*, 52(9):1211–1228.

Mulder, W. A. and Hak, W. (2009). Simultaneous imaging of velocity and attenuation perturbations from seismic data is nearly impossible. In *Extended Abstracts, 71st Conference and Technical Exhibition*. EAGE. S043.

Pratt, R. (1999). Seismic waveform inversion in the frequency domain, part 1: Theory and verification in a physical scale model. *Geophysics*, 64:888–901.

Ribodetti, A., Gaffet, S., Operto, S., Virieux, J., and Saracco, G. (2004). Asymptotic waveform inversion for unbiased velocity and attenuation measurements: numerical tests and application for vesuvius lava sample analysis. *Geophysical Journal International*, 158:353–371.

Ribodetti, A. and Virieux, J. (1998). Asymptotic theory for imaging the attenuation factor Q. *Geophysics*, 63(5):1767–1778.

Robertsson, J. O. A., Blanch, J. O., and Symes, W. W. (1994). Viscoelastic finite-difference modeling. *Geophysics*, 59(9):1444–1456.

Sirgue, L. and Pratt, R. G. (2004). Efficient waveform inversion and imaging: A strategy for selecting temporal frequencies. *Geophysics*, 69(1):231–248.

Takam Takougang, E. M. and Calvert, A. J. (2011). Application of waveform tomography to marine seismic reflection data from the Queen Charlotte Basin of western Canada. *Geophysics*, 76(2):B55–B70.

Tarantola, A. (1984). Inversion of seismic reflection data in the acoustic approximation. *Geophysics*, 49:1259–1266.

Tarantola, A. (1986). Theoretical Background for the Inversion of Seismic Waveforms, Including Elasticity and Attenuation. *Pure and Applied Geophysics*, 128(1/2):365–399.

Versteeg, R. (1994). The Marmousi experience: Velocity model determination on a synthetic complex data set. *The Leading Edge*, 13:927–936.

Virieux, J. and Operto, S. (2009). An overview of full-waveform inversion in exploration geophysics. *Geophysics*, 74(6):WCC1–WCC26.